NANO LETTERS

Letter

pubs.acs.org/NanoLett

Dynamic Nuclear Spin Polarization of Liquids and Gases in Contact with Nanostructured Diamond

Daniel Abrams,[†] Matthew E. Trusheim,[§] Dirk R. Englund,[§] Mark D. Shattuck,[†,‡] and Carlos A. Meriles*[,†]

[†]Department of Physics and [‡]Benjamin Levich Institute, CUNY-City College of New York, New York, New York 10031, United States

[§]Department of Electrical Engineering and Computer Science, Massachusetts Institute of Technology, Cambridge, Massachusetts 02139, United States

Supporting Information

ABSTRACT: Optical pumping of spin polarization can produce almost complete spin order but its application is restricted to select atomic gases and condensed matter systems. Here, we theoretically investigate a novel route to nuclear spin hyperpolarization in arbitrary fluids in which target molecules are exposed to polarized paramagnetic centers located near the surface of a host material. We find that adsorbed nuclear spins relax to positive or negative polarization depending on the average paramagnetic center depth and nanoscale surface topology. For the particular case of optically pumped nitrogen-vacancy centers in diamond, we calculate strong nuclear spin polarization at moderate magnetic fields provided the crystal surface is engineered with surface roughness in the few-nanometer range. The equilibrium nuclear spin temperature depends only weakly on the correlation time describing the molecular adsorption dynamics and is robust in the presence of other, unpolarized paramagnetic centers. These features could be exploited to polarize flowing liquids or gases, as we illustrate numerically for the model case of a fluid brought in contact with an optically pumped diamond nanostructure.

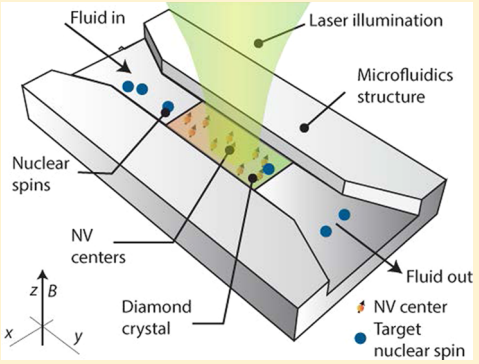

KEYWORDS: *Nitrogen-vacancy centers, nanostructured diamond, dynamic nuclear polarization, hyperpolarization, surface spin relaxation, microfluidics*

The nitrogen-vacancy (NV) center, a paramagnetic defect in diamond formed by a substitutional nitrogen and an adjacent vacancy, is emerging as a promising platform for a broad set of applications ranging from quantum information processing and spintronics, to nanoscale sensing.[1] Of particular interest herein are the so-called "shallow" NVs, that is, nitrogen-vacancy centers engineered just below the diamond surface via ion implantation[2] or CVD growth.[3] Recent work has shown that the spin of such centers can serve as a versatile nanoscale probe,[4] capable of detecting, for example, the nuclear spin field created by molecules on the diamond surface.[5,6] Here we investigate a complementary application where, rather than acting as a sensor, the NV is engineered and manipulated to serve as the source of nuclear spin relaxation. For shallow NVs continuously pumped into a predefined spin state, we show that the magnetic fluctuations arising from molecular surface hopping drive adsorbed nuclear spins into a quasi-equilibrium state of athermal polarization. The sign and amplitude of this polarization is a sensitive function of the NV depth and surface geometry. In particular, we find that nanoscale roughness at the interface separating the NVs from the adsorbed molecules plays a key role in making nuclear spin relaxation sufficiently strong. For a given surface topology, the resulting nuclear magnetization changes sign as we gradually displace the NVs toward the diamond surface. Using microfluidic modeling we build on the above results to show that substantial nuclear spin polarization can be attained by flowing the molecules of a gas or a liquid across an optically pumped diamond nanostructure. We refer to the proposed technique as NV-driven dynamic nuclear polarization or NV-DNP.

To model the dynamics of spin relaxation between paramagnetic centers and nuclear spins in a fluid, we start by considering the "diamond spin pump" geometry of Figure 1a. Shallow NVs within a "source" diamond crystal are continuously driven into the state $m_S = 0$ of the NV ground state triplet via green light illumination.[7] A dc magnetic field B normal to the crystal surface and coincident with the NV symmetry axis breaks the degeneracy between the $m_S = \pm 1$ states. A microfluidic structure brings the molecules of a "target" gas or liquid into contact with the source crystal. A fraction of these molecules is temporarily adsorbed onto the diamond surface causing a dipolar magnetic interaction with the NVs. As molecules sample different positions within the surface, this interaction randomly evolves in time with a characteristic "correlation time" τ_c. For a sufficiently dilute collection of NV centers, the dynamics can be simplified to that

Received: January 13, 2014
Revised: March 29, 2014
Published: April 22, 2014

   dx.doi.org/10.1021/nl500147b | *Nano Lett.* 2014, 14, 2471−2478

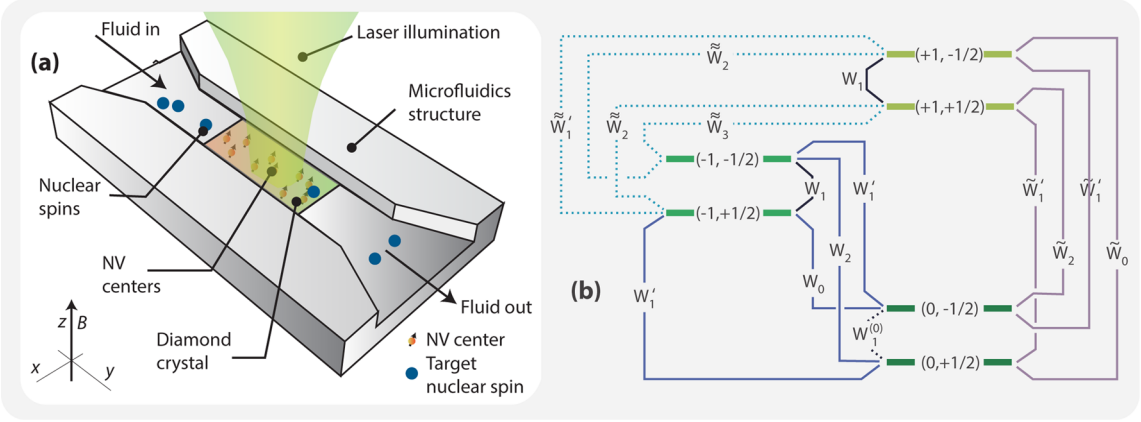

Figure 1. Fundamentals of NV-DNP. (a) Schematics of a "diamond spin pump". The fluid circulating through a microfluidics channel is steered toward the surface of a diamond crystal engineered to host near-surface NV centers. Laser illumination (and MW pulses, see text) are used to define a steady-state NV polarization. A permanent magnetic field B is applied along the z-axis, normal to the crystal surface and assumed to coincide with the NV direction. (b) Energy diagram of a spin pair comprising a NV center ($S = 1$) in the ground state and a nuclear spin ($I = 1/2$). The level notation follows the convention (m_S, m_I), where m references the projection of the spin angular momentum along z, as usual. $W_{|\Delta m_S+\Delta m_I|}$ indicates the transition probability between two levels separated by (Δm_S, Δm_I). Solid and dashed lines respectively indicate dipolarly allowed and forbiden transitions.

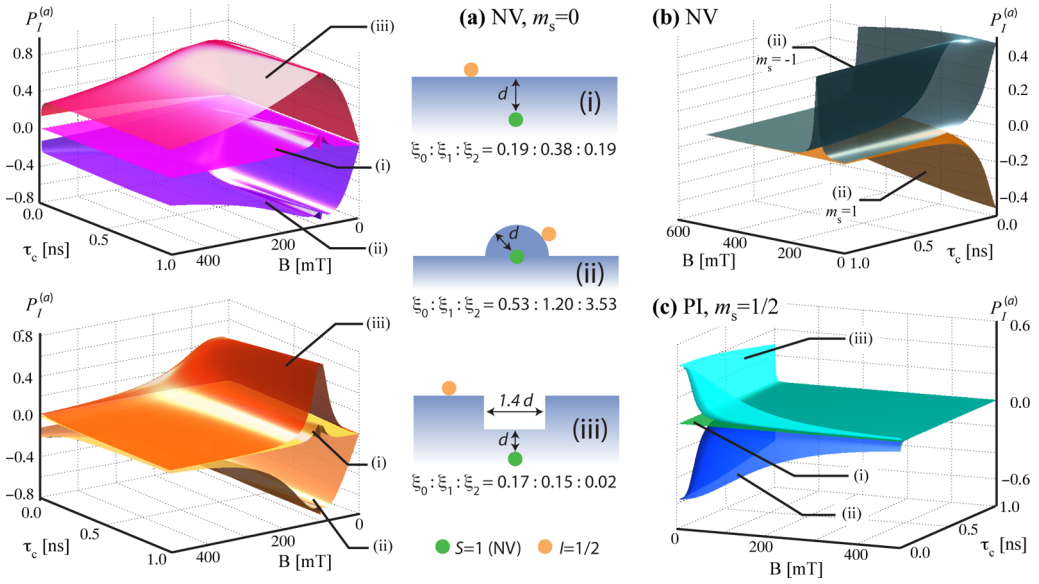

Figure 2. Steady-state polarization of adsorbed nuclear spins. (a) Polarization of nuclear spins on the diamond surface $P_I^{(a)}$ as a function of the applied magnetic field B and correlation time τ_c for an NV continuously pumped into $m_S = 0$ (as calculated from eq S6 in Supplementary Section S1). We assume three alternate geometries as described in the figure cartoon. All transition probability amplitudes ξ_j, j = 1,2,3, have been expressed in units of $(\pi\hbar^2k^2)/(Az^4)$, see main text for notation. (Top) Calculated $P_I^{(a)}$ assuming negligible intrinsic nuclear relaxation rate $1/T_{1I}^{(a)}$. (Bottom) Same as above but for the case where $1/T_{1I}^{(a)} = (W_2 + W_0 + \tilde{W}_2 + \tilde{W}_0)_m$. (b) Nuclear spin polarization when the NV state is $m_S = -1$ (dark green curve) or $m_S = 1$ (dark yellow curve). In both cases, it is assumed that the NV is at the base of a dome as described in (a) (geometry (ii)). (c) Same as in (a) but for the case when the NV is replaced by a paramagnetic impurity (PI) with spin number $S = 1/2$ and polarized to $m_S = 1/2$. In (b,c), the intrinsic nuclear spin relaxation rate is assumed to be negligible.

of individual spin pairs (Supporting Information Section S1) in the present case formed by an NV and a nuclear spin $I = 1/2$. Figure 1b shows the corresponding energy diagram, including the transition probabilities between states.

Ignoring for now molecular exchange with the bulk of the fluid, detailed balance between the populations in the different energy levels yields the steady-state polarization of adsorbed nuclear spins (see Supporting Information Section S1)

$$P_I^{(a)}(m_S = 0) \cong -\frac{(W_2 - W_0)}{\left(W_2 + W_0 + \frac{1}{T_{1I}^{(a)}}\right)} \quad (1)$$

where $1/T_{1I}^{(a)}$ is the nuclear spin relaxation rate on the diamond surface due to processes other than the interaction with the NVs. In the above expression the transition rates have the form $W_j = (\xi_j\tau_c)/(1 + ((\omega_{NV}^{(-1)} - (-1)^{j/2}\omega_I)\tau_c)^2)$ for j = 0,2 with τ_c denoting the correlation time of the adsorbed molecules; $\omega_I = \gamma_I B$ is the nuclear Zeeman frequency, $\omega_{NV}^{(-1)} = |\omega_{crys} - |\gamma_S|B|$ is the $m_S = 0 \rightarrow m_S = -1$ NV transition frequency with $\omega_{crys} = 2\pi$

dx.doi.org/10.1021/nl500147b | Nano Lett. 2014, 14, 2471−2478

× 2.87 GHz, the zero field splitting of the NV ground state, and γ_I (γ_S) denotes the nuclear (electronic) spin gyromagnetic ratio. Equation 1 is a simplified expression approximately valid when $\tau_c > 0.2$ ns and $B > 30$ mT, which are typical conditions; a formula valid for all correlation times and magnetic fields is presented in Supporting Information Section S1. ξ_j with $j = 0,2$ are constants quantifying the efficiency of the NV-induced nuclear spin relaxation, which depends strongly on the geometry governing the interaction between the NV and adsorbed nuclear spins. If the crystal is flat on a scale much larger than the NV distance to the surface (referred to as case (i)), a straighforward calculation assuming dipolar coupling shows that $\xi_0^{(i)} = \xi_2^{(i)} \cong 0.19\chi$, where $\chi \equiv \pi\hbar^2k^2/Az^4$, z is the NV distance to the surface, $k \equiv \mu_0\gamma_I\gamma_S/4\pi$, and $1/A \equiv \sigma$ is the NV surface density (Supporting Information Section S2). Since typically $\omega_{NV}^{(-1)} \gg \omega_I$, W_2 and W_0 converge to similar values so that the steady-state polarization, proportional to the difference between the two, is greatly diminished.

This cancellation, however, is a fortuitous consequence of the angular dependence governing the spin dipolar interactions between the NV and adsorbed nuclei and can be altered by changing the system geometry. One possibility is to align the magnetic field with the NVs whose axes are not perpendicular to the crystal surface (Supporting Information Section S2). Here, however, we are particularly interested in the effect of surface topology. In Figure 2a, we plot $P_I^{(a)}(m_S = 0)$ as a function of the applied magnetic field B and correlation time τ_c for three different configurations, where the NV is below a flat surface (case (i)), a dome (case (ii)), or a cylindrical pit (case (iii)). For simplicity, the top set of curves corresponds to the case where $1/T_{1I}^{(a)} \sim 0$.

Figure 2a shows a remarkable change in the polarization amplitude and a sign reversal as the diamond surface evolves from a convex to a concave geometry (cases (ii) and (iii), respectively). The maximum nuclear spin order is attained near $B_c = 100$ mT, where $\omega_{NV}^{(-1)}$ is minimum, but substantial nuclear polarization persist over a broad range of magnetic fields and correlation times. We note that level-anticrossing effects near B_c. not contemplated here, may lead to localized deviations from the presented model.[8] These, however, are restricted to a narrow interval (of order ±5 mT or less in ^{13}C-depleted diamond) and will be ignored in the remainder of the text.

In practice, adsorbed nuclear spins simultaneously experience multiple relaxation mechanisms, most importantly due to interactions with other, unpolarized paramagnetic centers within the diamond crystal. To assess the influence of these mechanisms on the adsorbed nuclear spins, we recalculate $P_I^{(a)}(m_S = 0)$ in the case where $1/T_{1I}^{(a)}$ is comparable to $(W_2 + W_0)_m$, where the subscript references the maximum NV-induced relaxation rate (bottom set of curves in Figure 2a). We find that the polarization buildup is now restricted to a narrower range of magnetic fields, the effect being substantially more pronounced for the concave geometry (case (iii)). The latter is a direct consequence of the comparatively weaker NV-induced relaxation in this configuration: A calculation (Supporting Information Section S2) shows that the constants governing the transition probability amplitudes in a pit-like geometry are respectively given by $\xi_0^{(iii)} = 0.17\chi$ and $\xi_2^{(iii)} = 0.02\chi$. By contrast, a convex topology in the form of a dome yields $\xi_0^{(ii)} = 0.53\chi$ and $\xi_2^{(ii)} = 3.53\chi$. Therefore, while the ratio $|(\xi_2 - \xi_0)/(\xi_2 + \xi_0)| \sim 0.75$ is comparable in both instances, the values $|\xi_2 \pm \xi_0|$ are approximately 20 times greater in case (ii), making this convex geometry less sensitive to other, coexisting paths of nuclear spin relaxation.

Although our discussion so far has been restricted to the case where the NV is selectively pumped into $m_S = 0$ of the ground state triplet, it is interesting to consider an alternate scenario where the NV population is steadily driven into, for example, $m_S = -1$. Experimentally, this could be accomplished by concatenating intervals of laser excitation with selective microwave inversion pulses. Detailed balance yields in this case (Supporting Information Section S1)

$$P_I^{(a)}(m_S = -1) = \frac{(W_2 - W_0)}{\left(W_2 + 2W_1 + W_0 + \frac{1}{T_{1I}^{(a)}}\right)} \quad (2)$$

with $W_1 = (\xi_1\tau_c)/(1 + \omega_I\tau_c)^2$. By the same token and assuming selective NV pumping into $m_S = +1$, we obtain

$$P_I^{(a)}(m_S = +1) = -\frac{(\tilde{W}_2 - \tilde{W}_0)}{\left(\tilde{W}_2 + 2W_1 + \tilde{W}_0 + \frac{1}{T_{1I}^{(a)}}\right)} \quad (3)$$

where $\tilde{W}_j = (\xi_j\tau_c)/(1+((\omega_{NV}^{(+1)}-(-1)^{j/2}\omega_I)\tau_c))$ with $j = 0,2$ and $\omega_{NV}^{(+1)} = \omega_{crys} + |\gamma_S|B$. A plot of eqs 2 and 3 as a function of the magnetic field and correlation time is presented in Figure 2b for the geometry of case (ii) and in the absence of intrinsic nuclear spin relaxation ($1/T_{1I}^{(a)} \sim 0$). Relative to the top set of curves in Figure 2a, we observe major changes in $P_I^{(a)}$ including a sign reversal and a redistribution of the nuclear spin polarization into a narrower range around B_c (for NV pumping into $m_S = -1$) or toward shorter correlation times (when $m_S = +1$). The overall conclusion is that NV pumping into $m_S = 0$ is not only the simplest way to induce nuclear spin alignment but presumably the most efficient.

It is of interest to study closely the influence of other paramagnetic defects on $P_I^{(a)}$. Particularly important is the role of substitutional nitrogen (also called P1 center), a paramagnetic impurity (PI) of spin number 1/2. Because most NV conversion protocols have only a fractional yield,[9] nitrogen impurities are present in all NV-doped surfaces, typically at a higher concentration. Conceivably, P1 centers can be dynamically polarized via contact with optically pumped NVs,[10,11] and thus can themselves contribute to aligning adsorbed nuclear spins. Figure 2c shows the predicted nuclear spin polarization for a model where nuclear spin relaxation is governed by spin-1/2 paramagnetic centers polarized to $m_S = +1/2$ (Supporting Information Section S3). Not surprisingly, we find a dependence on the surface topology comparable to that of Figure 2a; because of the absence of a crystalline field, however, dynamic nuclear polarization is restricted to shorter correlation times and lower magnetic fields. This behavior is of interest not only when paramagnetic impurities drive nuclear alignment but perhaps more importantly when unpolarized PIs compete against polarized NVs. In this latter case, we model the relaxation rate of adsorbed nuclei as $1/T_{1I}^{(a)} \sim (W_2 + 2W_1 + W_0)^{(PI)}$ where the superscript indicates that the transition probabilities are those due to a spin-1/2 paramagnetic defect (Supporting Information Section S3). Because of the distinct dependence on τ_c and B, the polarization loss, captured by the factor $[T_{1I}^{(a)}(W_2 + W_0)^{(NV)}]^{-1}$, can be mitigated via an adequate selection of the working conditions (that is, magnetic field, temperature, surface roughness, and so forth). In other words, the detrimental effect of unpolarized PIs on the dynamical polarization of adsorbed nuclear spins can be significantly

dx.doi.org/10.1021/nl500147b | Nano Lett. 2014, 14, 2471−2478

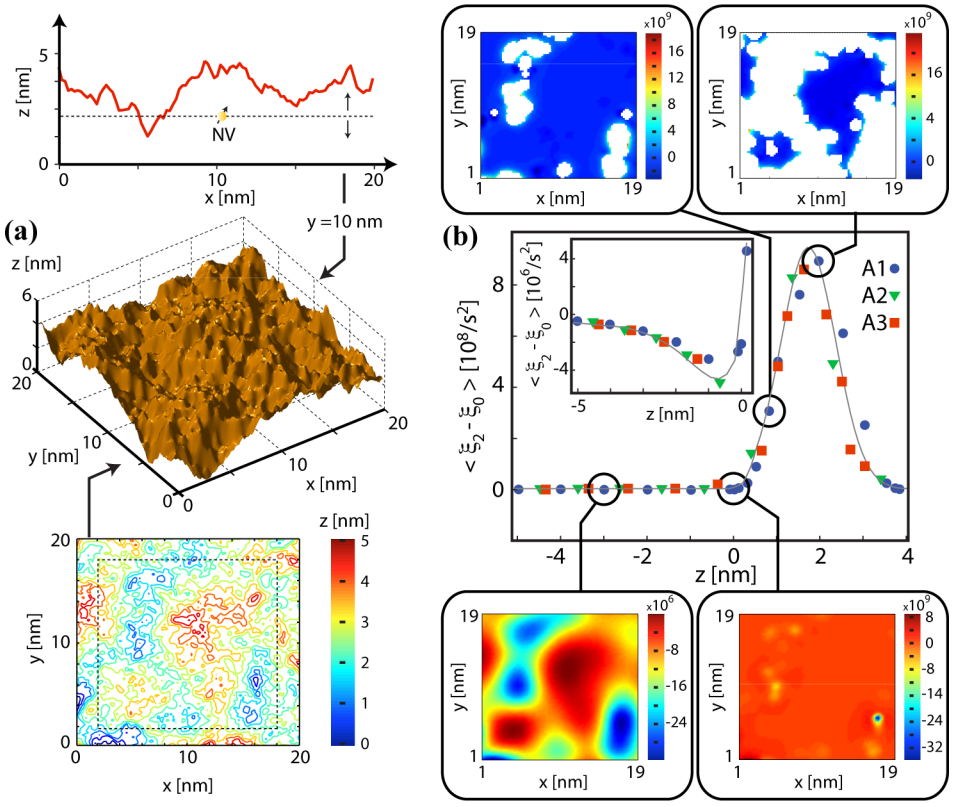

Figure 3. Topology-dependent NV-DNP. (a) Code-generated diamond surface, hereafter identified as A1, exhibiting nanoscale roughness (center); the height difference between the highest and lowest point (at $z = 0$) is 5 nm. The surface contour plot (bottom) and a cross section at $y = 10$ nm (top) are included for clarity. In our calculations, we determine the average value of $\xi_2 - \xi_0$ as we displace the NV position across an imaginary, horizontal plane at a variable height z (dashed line on the cross section graph, dashed square in the contour plot). (b) $\langle \xi_2 - \xi_0 \rangle$ as a function of depth for three different, randomly generated surfaces (denoted as A1, A2, and A3) with the same roughness spectral density. The insert in the main figure zooms on the calculated response for deeper values of z. In all cases, symbols are calculated data points and the fainted gray line is a guide to the eye. The side inserts show the calculated maps of $\xi_2 - \xi_0$ corresponding to surface A1 at four different depths. In all calculations the NV surface density is $\sigma = 10^{12}$ cm^{-2}.

suppressed, even for comparatively greater concentrations of paramagnetic defects (Supporting Information Section S3).

A question of practical importance in the implementation of NV-DNP is how to best engineer the surface topology. From the results in Figure 2, we conclude that a convex geometry is among the most favorable but arraying a set of NV-hosting, nanometer-sized domes is challenging with present technology. In Figure 3, we model an arguably more realistic scenario where engineered NVs occupy random positions across a horizontal plane of arbitrary height z along the surface normal; under this assumption, a smaller fraction of the plane becomes available to the NVs as z becomes greater than z_{min}, the height at the deepest valley point. Such configuration could be attained, for example, by controllably etching the surface of a delta-doped diamond.[4] For the present calculations we assume that the roughness amplitude along the surface-normal amounts to 5 nm (and choose the reference frame so that $z_{max} = 5$ nm and $z_{min} = 0$ nm). To account for the deleterious effect of bandgap-bending,[12] we also assume that the NVs become inactive once the distance to the surface falls below 0.7 nm.

Provided complete optical pumping of the NV into the $m_S = 0$ state, we obtain a direct measure of the nuclear spin polarization efficiency via $\xi_2 - \xi_0$, the difference between transition rate constants, which we calculate in Figure 3b as the NV position is varied across a given horizontal plane at a fixed height z. For NVs deep below the diamond surface (that is, when $z < 0$), we find that $\xi_2 - \xi_0$ closely follows the surface topography. This can be most clearly seen by considering the map at $z = -3$ nm (lower left insert in Figure 3b), where $\xi_2 - \xi_0$ takes negative values below the valleys but turns positive underneath the crests (geometries corresponding to cases (iii) and (ii) in Figure 2a, respectively). Overall, the average $\langle \xi_2 - \xi_0 \rangle$ over the entire plane is negative below $z = 0$ (insert within main plot in Figure 3b) because NVs are preferentially closer to nuclear spins in the surface valleys. As the NV depth is increasingly reduced, $\xi_2 - \xi_0$ preferentially turns to positive, resulting in positive averages when $z > 0$ (main plot). The change abruptly occurs on a scale of just ~3 nm. An identical trend was observed after replacing the model surface of Figure 3a by other similar code-generated surfaces (green triangles and red squares in the main plot), implying that the calculated averages are representative of this type of surface as a whole. Interestingly, the positive section of the calculated curve (with maximum at $z \approx 2$ nm) completely dwarfs the negative tail (with minimum at $z \approx -1$ nm), which we interpret as a direct consequence of the greater values adopted by $\xi_2 - \xi_0$ in a convex geometry and near hillsides and cliffs (Supporting Information Section S2). The latter is implicit in the maps of $\xi_2 - \xi_0$ at $z > 0$ (upper inserts in Figure 3b), where we observe large, positive contributions near the white patches (that is, sections where the NVs collapse due to proximity to the surface).

dx.doi.org/10.1021/nl500147b | *Nano Lett.* 2014, 14, 2471−2478

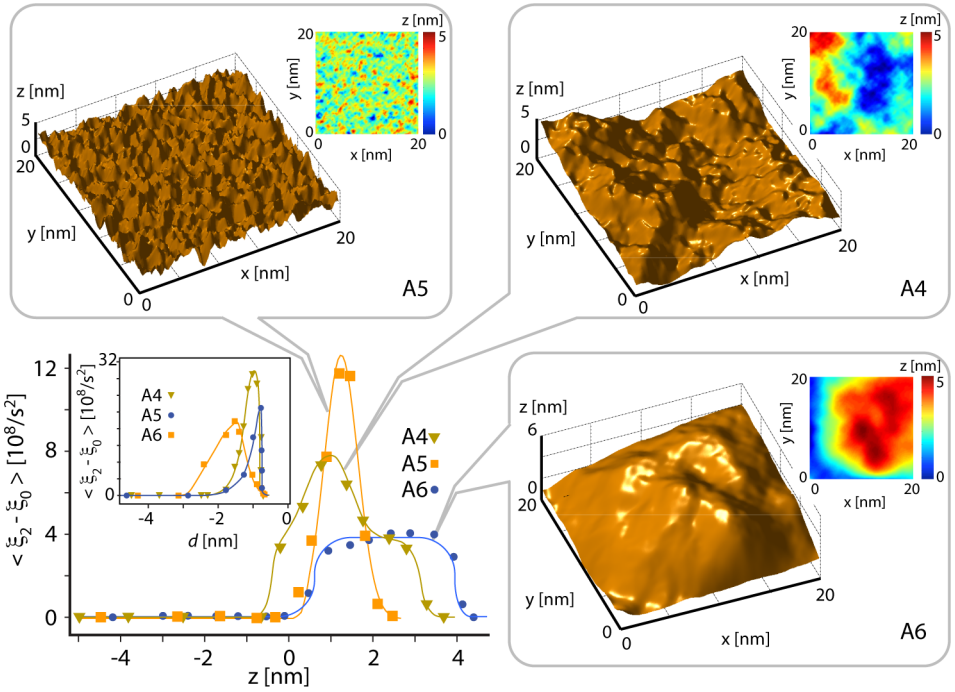

Figure 4. The influence of surface roughness on the nuclear spin polarization efficiency. (Main) $\langle \xi_2 - \xi_0 \rangle$ as a function of the vertical position z of the NV plane for three code-generated surfaces. The height difference between the highest and lowest points in each surface is 5 nm, but the nanometer roughness changes from high (A5), to medium (A4), to low (A6). (Insert) $\langle \xi_2 - \xi_0 \rangle$ assuming that rather than on a horizontal plane of fixed height the NV is a distance d below the surface. Symbols represent calculated data points and the lines are guides to the eye. The assumed NV surface density is $\sigma = 10^{12}$ cm^{-2}.

The predominant configuration between shallow NVs and adsorbed nuclei (and thus the range and maximum amplitude of $\langle \xi_2 - \xi_0 \rangle$) may be controlled by the experimenter by optimizing the surface roughening. This is shown in Figure 4 where, for illustration purposes, we calculate $\xi_2 - \xi_0$ for three new code-generated surfaces. As in Figure 3, the roughness amplitude is chosen to be 5 nm, but the code is modified to alter the frequency and spread of the valleys and crests throughout the surface. We find that $\langle \xi_2 - \xi_0 \rangle$ reaches a higher maximum when the surface is more rugged (upper left insert in Figure 4). The positive section of the curve, however, spreads over a narrower range, which in practice would make this topography more susceptible to NV misplacement. We observe the exact opposite as we generate smoother-looking surface features (A4 and A6 on the right of Figure 4) with a mesa-like behavior emerging for surface A6.

Whether to introduce surface roughness before or after NV implantation will depend on a number of factors throughout the various surface preparation steps. Material processing considerations notwithstanding, the answer is not obvious when the analysis is restricted to the surface topology: When the NVs are distributed over a horizontal plane (as assumed thus far), deep surface roughening selectively removes the color centers near the valleys (where $\xi_2 - \xi_0$ is negative), presumably leading to stronger NV-DNP. The insert plot in the central panel of Figure 4 demonstrates, however, that this argument is deceiving. Here we recalculate $\langle \xi_2 - \xi_0 \rangle$ for the same three model surfaces. Unlike the main plot, we assume this time that the NVs have been implanted at a uniform depth d relative to the local height $z(x, y)$ of the roughened diamond surface. We find a remarkable change in the overall behavior toward a sharper dependence on NV position and higher maxima. We observe a reversal of the trend in the main plot, with more coarsely grained surfaces leading to greater $\langle \xi_2 - \xi_0 \rangle$ values.

NV surface density and implantation depth are additional practical considerations. NV centers engineered as close as 1 nm from the surface have been shown to retain the relatively long coherence lifetimes required for spin sensing.[13] Similar fabrication protocols could be adapted to the present application so as to create dense layers of near-surface NVs. We emphasize, however, that the spin−lattice relaxation times T_{1S} governing the NV dynamics (typically 100 μs in nanocrystals[14] and up to 10 ms in high-purity bulk crystals[15]) need only be longer than the correlation time τ_c characterizing molecular hopping on the diamond surface (anticipated to be much shorter, see below). Thus, NV surface densities exceeding 10^{12} cm^{-2} at a depth of 1−2 nm below the surface are realistic in the present application without any immediate deleterious effect.

The numerical modeling of the nuclear spin polarization of a fluid partly relies on the assumed correlation time, which depends on the physics governing the dynamics of the target molecules near the diamond surface. Adsorbed molecules in gases, for example, hop from one site to the next during a dwell time $\tau_a \gg \tau_c$ until finally desorbing from the surface. The fractional time $f = \tau_a/\tau_b$ that a molecule spends on the solid relative to the time τ_b in the bulk of the fluid is a thermally activated function that depends on the surface potential (and thus on the surface roughness and termination) of the particular solid surface under investigation. This type of dynamics is observed, for example, in the study of optically pumped alkali vapors, where the correlation time τ_c, which in this case governs the interaction of nuclear spins in the vapor with paramagnetic defects on the surface of the glass container, can be quite long for typical operation conditions.[16]

dx.doi.org/10.1021/nl500147b | Nano Lett. 2014, 14, 2471−2478

The dynamics of molecules at a solid−liquid interface are less understood. Several studies have demonstrated how solids induce order in adjacent fluids but various boundary conditions are invoked, ranging from the no-slip condition, where the liquid is static relative to the solid at the surface, to pure slip, to multilayer locking.[17] While a detailed discussion is beyond the scope of this work, we assume that the relevant processes at the solid−liquid interface can be described via an effective correlation time $\tau_c \geq 0.1$ ns. This assumption is justified by noting that for NVs sufficiently close to the surface, the unit time probabilities $W_j \propto 1/z^4$ are non-negligible over a range of a few nanometers, where the dynamics transitions from quasi-static (on the surface) to mobile (in the fluid).[18] Determining the exact correlation time is largely unnecessary because as shown in Figure 2 the steady-state nuclear spin polarization is rather insensitive to τ_c (at least for $\tau_c \geq 0.1$ ns). Further, the existence of a correlation time does not have direct implications on the type of trajectories molecules follow on the surface (for example, discrete or continuous hops), implying that our formulas apply both to liquids and gases (Supporting Information Section S2).

Building on the above considerations, we now proceed to model the dynamic polarization of a bulk fluid brought into close proximity with shallow NVs optically pumped into $m_S = 0$. Figure 5a introduces a possible geometry: A microfluidic channel steers the target liquid or gas into an optically pumped diamond microstructure formed by two parallel diamond walls separated by 0.5 μm. We assume that the NV depth and nanoscale roughness of the diamond surface is chosen to optimize $\langle \xi_2 - \xi_0 \rangle$, as described in Figures 3 and 4. To estimate the efficiency, we start by calculating the fluid polarization in the absence of flow. In this limit and assuming that the NVs are pumped into $m_S = 0$, the formula for bulk nuclear spin polarization takes the approximate form (Supporting Information Section S4)

$$(P_I^{(b)})_{max} \approx -f T_{1I}^{(b)} (W_2 - W_0) \quad (4)$$

where $T_{1I}^{(b)}$ is the nuclear spin−lattice relaxation time of molecules removed from the walls, and the fractional time satisfies the condition $f \ll 1$. For example, for a typical protonated solvent, where $T_{1I}^{(b)}$ is of the order of 5−10 s, one obtains $(P_I^{(b)})_{lim} \cong -10^{-2}$ for realistic surface conditions (Supporting Information Section S4). This latter value must be understood, however, as an upper bound since molecular diffusion away from the illuminated area during the buildup time (of order $T_{1I}^{(b)}$) necessarily reduces the final nuclear spin polarization. This is illustrated in Figure 5a, where the numerical integration of an adapted convection-diffusion equation (see Methods section) yields a peak proton polarization in water of 0.2%. This polarization is remarkably high considering that the thermal proton spin polarization in the assumed ∼100 mT field amounts to just 5×10^{-7}. Greater polarization levels may be possible in select gases, where $T_{1I}^{(b)}$ can be considerably longer than in a liquid, provided the target system can be properly confined during the pumping process.

In a practical application, a trade-off exists between the bulk polarization of the outgoing fluid and the flow rate. The critical parameter is the transit time τ_t across the NV-implanted region. This is shown in Figure 5b where we calculate the stationary nuclear spin polarization of proton spins in bulk water during transit and after exiting the diamond microstructure for two different flow rates. We find a level of polarization similar to

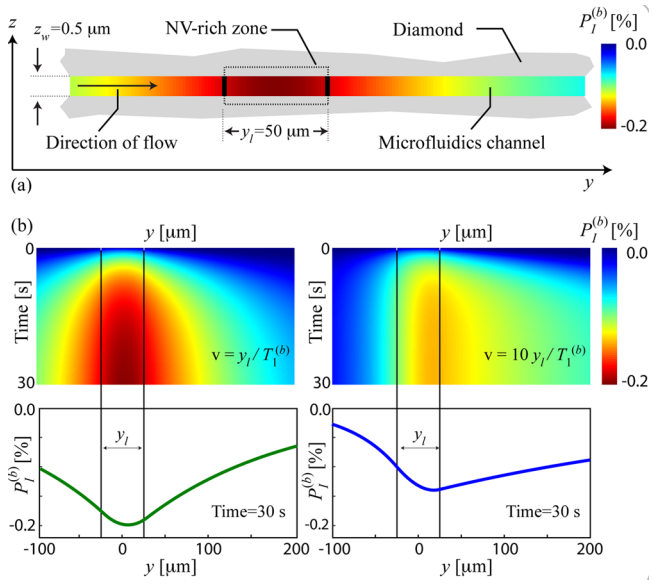

Figure 5. Modeling the polarization of fluids in a microfluidics device. (a) A 0.5 μm wide microchannel brings the fluid in contact with a 50 μm long diamond microstructure whose walls (assumed infinitely extended in the direction normal to the drawing) have been previosly implanted with NVs. For clarity, the vertical scale (channel width) is ten times larger than the horizontal scale (channel length). The color map is the calculated steady-state spatial distribution of proton polarization throughout the channel in the absence of flow ($v = 0$). (b) Calculated time-dependence of the proton polarization in water as a function of the position along the microchannel relative to the NV rich zone; the flow velocity is $v = y_I/T_{1I}^{(b)} = 5$ μm/s and $v = 10\ y_I/T_{1I}^{(b)} = 50$ μm/s in the left and right panels, respectively. The bottom curves represent the corresponding steady-state spatial profiles calculated 30 s after the laser is turned on. In all calculations, we assume that the NVs are continuously pumped into $m_S = 0$ and that $B = 110$ mT, $\tau_c = 10^{-9}$ s, and $T_{1I}^{(b)} = 10$ s. The surface roughness as well as the NV depth (∼1 nm) and surface density ($\sim 10^{12}$ cm^{-2}) are chosen so as to yield $W_2 \sim 7W_0 \sim 1$ s^{-1}.

that obtained in Figure 5a when $\tau_t \approx T_{1I}^{(b)}$, though in the regime of continuous flow the polarized fluid can only be transported over a distance comparable to the size of the implanted region (of length y_I in the sketch of Figure 5a). The opposite applies for greater flow rates: the delivery range increases at the expense of the final bulk polarization. Transport of optimally polarized fluids over longer distances could be attained by illuminating a larger area (see below), by operating in batch mode, or by making the transport channel narrower than the polarization channel. Note that in Figure 5, the fluid polarization is approximately uniform throughout the channel width z_w (see polarization map in Figure 5a). The latter reflects the fact that the diffusion time $\tau_w \sim z_w^2/D$ in a fluid of self-diffusion coefficient D (∼100 μs for molecules in water, the model fluid in this example) is typically much smaller than the nuclear polarization time $\sim(W_2 + W_0)^{-1}$ (of order ∼1 s for the assumed magnetic field and surface conditions).

From eq 4 we conclude that the steady-state polarization in the fluid is largely dominated by the working geometry via the fraction of time $f \ll 1$ molecules spend in contact with the diamond surface. While further reducing the interwall separation in the channel is an obvious way to increase f, an alternate route is to enhance the overall surface via the use of 3D structures. For example, plasma etching techniques already introduced for the scalable fabrication of nanowires[19] and

dx.doi.org/10.1021/nl500147b | Nano Lett. 2014, 14, 2471−2478

nanocrystals[20] from single diamond crystals could be adapted to produce a set of vertical pillars randomly distributed throughout an otherwise flat microfluidic channel. Along the same lines, one can envision systems where the fluid permeates through diamond nanocrystals arrayed in a packed-bed-type geometry. Further work will be required, however, to account for the probabilistic alignment between the NV axis and the applied magnetic field.

The volume of maximally polarized fluid that can be generated per unit time largely depends on the size of the optically pumped area, which for the vertical illumination assumed in Figure 5 would be restricted to less than ~$(30-50\ \mu m)^2$ for reasonable laser intensities (~1 mW/μm^2 are typically required to pump NV centers on the microsecond time scale). Geometries where light is injected laterally into thin diamond sheets of larger surface area are, however, a conceivable way to circumvent this limitation, especially if the sheets are embedded within cavity-like structures designed to reflect and redistribute light efficiently throughout the entire surface.

NV-DNP could circumvent several complications found in other hyperpolarization schemes. For example, unlike in para-hydrogen-based methods,[21,22] no chemical reaction is required, which also makes the polarization transfer insensitive to the chemical structure of the target molecule (thus eliminating the typical antiphase doublets in the resulting NMR spectra). NV-DNP shares the same hyperpolarization principles governing dissolved radicals[23] or semiconductor nanoparticles[24] but the presence of a zero-field splitting and efficient NV spin optical pumping make this approach of special interest. Dynamic nuclear polarization of atomic and molecular gases is particularly intriguing because the fraction of molecules adsorbed on the diamond surface, and thus the concomitant nuclear spin polarization, see eq 4, can be greatly enhanced by moderately reducing the gas temperature.

NV-DNP can be extended in several ways including the use of Hartman–Hahn protocols to polarize near-surface paramagnetic impurities[10] or ^{13}C spins[25], which can then cross-relax with the nuclear spin of the fluid. For example, delta doping, diamond overgrowth, and surface termination could be combined to create ultrapure ^{13}C-enriched films capable of transferring polarization to the outside fluid without the need for a direct coupling with the NV layer; further work, however, is needed to assess the efficiency of these or similar schemes. By the same token, paramagnetic defects other than the NV center could also serve as polarization sources; examples include the divacancy and silicon-vacancy centers in SiC,[26,27] and rare-earth ions in YAG.[28]

Finally, it is worth highlighting the relative simplicity of the hardware required in a practical implementation: Unlike the most advanced forms of DNP, requiring sophisticated microwave instrumentation, a freeze–thaw cycle, and a sample-shuttling protocol,[29,30] an NV-DNP system would take the form of a compact optofluidic chip within a benchtop magnet. This versatility could pave the way to numerous applications including laboratory and point-of-care diagnostics, combinatorial synthesis and screening, food safety, environmental testing, scientific studies of mass-limited systems, and the detection of hazardous biochemical agents.

Methods. To model spin transport in the microfluidics structure, we first note that the diffusion time across the width $z_w = 500$ nm of the channel for a fluid such as water is $\tau_w = z_w^2/D = 109\ \mu s$ (the self-diffusion coefficient for water is $D = 2.3 \times 10^{-9}\ m^2/s$). Since arguably $\tau_w \ll |W_2 \pm W_0|^{-1} < T_{1I}^{(b)}$ we look for solutions where the proton polarization $\langle I\rangle(z, y, t) \cong \langle\bar{I}\rangle(y, t) \equiv 1/z_w \int_0^{z_w}\langle I\rangle(z, y, t)dz$ is independent of z. In this limit, the spin transport equation for NVs pumped onto $m_S = 0$ in a magnetic field $B = 110$ mT reduces to (Supporting Information Section S4)

$$\frac{d\langle\bar{I}\rangle}{dt}(y, t) = -\langle\bar{I}\rangle(y, t)\left(\frac{1}{\hat{T}_{1I}^{(NV)}(y)} + \frac{1}{T_{1I}^{(a)}(y)} + \frac{1}{T_{1I}^{(b)}}\right) - \frac{S_0}{T_{1I}^{(NV)}(y)} - \frac{2v}{3}\frac{\partial\langle\bar{I}\rangle}{\partial y}(y, t) + D\frac{\partial^2\langle\bar{I}\rangle}{\partial y^2}(y, t) \quad (5)$$

where $1/T_{1I}^{(NV)} \approx f_{eff}(W_2 - W_0)|_{z_0}\theta(|y| - y_l/2)$, $1/\hat{T}_{1I}^{(NV)} \approx f_{eff}(W_2 + W_0)|_{z_0}\theta(|y| - y_l/2)$, $1/T_{1I}^{(a)} \approx f_{eff}W^{(PI)}\theta(|y| - y_l/2)$, $\theta(y)$ is the Heaviside function, z_0 is the NV distance to the surface, $f_{eff} = ((2z_0)/(3z_w))(1 - z_0^3/(z_w + z_0)^3)$ is the effective fraction of molecules in contact with the surface, $2v/3$ is the average velocity across the channel, and we have chosen the origin of the reference frame to coincide with the midpoint of the implanted section of the channel, of length y_l. We solve eq 5 and determine the bulk fluid polarization $P_I^{(b)}(y,t) \equiv 2\langle\bar{I}\rangle(y,t)$ numerically using finite-difference forward integration over a large domain L in y to approximate boundaries at infinity. The results for $P_I^{(b)}(y,t)$ near the NV rich central region with $\langle S_0\rangle = 1/2$, $z_0 = 1$ nm, $y_l = 50\ \mu m$, $L = 1.6$ mm, $f_{eff} = 1.3 \times 10^{-3}$, $T_{1I}^{(b)}$=10 s, $W_2|_{z_0} = 1\ s^{-1}$, $W_0|_{z_0} = 0.15\ s^{-1}$, and $W^{(PI)} = 1\ s^{-1}$ at two flow velocities $v = y_l/T_{1I}^{(b)} = 5\ \mu m/s$ and $v = 10\ y_l/T_{1I}^{(b)} = 50\ \mu m/s$ are shown in Figure 5b. The limit steady-state polarization possible in a channel whose length L coincides with the length of the implanted section y_l is $(P_I^{(b)})_{lim} = -f_{eff}(W_2 - W_0)/(f_{eff}(W_2 + W_0 + W^{(PI)}) + 1/T_{1I}^{(b)}) \approx -1.1\%$, which is roughly a factor of 6 larger than the maximum of 0.2% seen in the simulation. Thus, molecular diffusion plays a significant role in reducing the polarization in a long channel. In fact, it is possible to determine the approximate ($(P_I^{(b)})_{lim} \ll 1$) steady-state solution $P_I^{(b)}(y)$ for eq 5 if $v = 0$. One finds:

$$P_I^{(b)}(y) = \begin{cases} (P_I^{(b)})_{lim}\left(1 - \exp\left(-\frac{y_l/2}{\sqrt{DT_{1I}^{(b)}}}\right)\right)\cosh\left(\frac{y}{\sqrt{DT_{1I}^{(b)}}}\right) & \text{if } |y| \le \frac{y_l}{2} \\ (P_I^{(b)})_{lim}\sinh\left(\frac{y_l/2}{\sqrt{DT_{1I}^{(b)}}}\right)\exp\left(\frac{-|y|}{\sqrt{DT_{1I}^{(b)}}}1\right) & \text{if } |y| > \frac{y_l}{2} \end{cases} \quad (6)$$

dx.doi.org/10.1021/nl500147b | Nano Lett. 2014, 14, 2471–2478

Thus, the limit polarization in an infinite channel is $(P_I^{(b)})_{lim}(1-\exp(-y_I/(4DT_{1I}^{(b)})^{1/2})) \approx -0.2\%$ in agreement with the simulation.

■ ASSOCIATED CONTENT

Supporting Information

Supporting Information is accompanying this manuscript including a detailed derivation of eqs 1−6 as well as a formal description of the influence of unpolarized spin-1/2 centers to the relaxation of nuclear spins on the diamond surface. This material is available free of charge via the Internet at http://pubs.acs.org.

■ AUTHOR INFORMATION

Corresponding Author

*E-mail: cmeriles@sci.ccny.cuny.edu.

Author Contributions

C.A.M. derived the analytical formulas. M.D.S., D.A., M.E.T., and D.E. carried out the numerical simulations. All authors contributed to analyzing the data and writing the paper.

Notes

The authors declare no competing financial interest.

■ ACKNOWLEDGMENTS

D.A. and C.A.M. acknowledge support from the National Science Foundation through Grants NSF-1111410 and NSF-1309640. M.T. acknowledges support from Grant NSF-0801525; D.E. acknowledges support from the DARPA YFA program. M.T. was supported by the NSF IGERT program Interdisciplinary Quantum Information Science and Engineering (iQuiSE). We are thankful to J. Wrachtrup, F. Jelezko, P. Neumann, and J. A. Reimer for helpful discussions.

■ REFERENCES

(1) Acosta, V.; Hemmer, P. *MRS Bull.* **2005**, *38*, 127.
(2) Pezzagna, S.; Wildanger, D.; Mazarov, P.; Wieck, A. D.; Sarov, Y.; Rangeow, I.; Naydenov, B.; Jelezko, F.; Hell, S. W.; Meijer, J. *Small* **2010**, *6*, 2117.
(3) Ohno, K.; Heremans, F. J.; Bassett, L. C.; Myers, B. A.; Toyli, D. M.; Bleszynski-Jayich, A. C.; Palmstrøm, C. J.; Awschalom, D. D. *Appl. Phys. Lett.* **2012**, *101*, 082413.
(4) Grinolds, M. S.; Hong, S.; Maletinsky, P.; Luan, L.; Lukin, M. D.; Walsworth, R. L.; Yacoby, A. *Nat. Phys.* **2013**, *9*, 215.
(5) Staudacher, T.; Shi, F.; Pezzagna, S.; Meijer, J.; Du, J.; Meriles, C. A.; Reinhard, F.; Wrachtrup, J. *Science* **2013**, *339*, 561.
(6) Mamin, H. J.; Kim, M.; Sherwood, M. H.; Rettner, C. T.; Ohno, K.; Awschalom, D. D.; Rugar, D. *Science* **2013**, *339*, 557.
(7) Manson, N. B.; Harrison, J. P.; Stellars, M. J. *Phys. Rev. B* **2006**, *74*, 104303.
(8) Wang, H. J.; Shin, C. S.; Avalos, C. E.; Seltzer, S. J.; Budker, D.; Pines, A.; Bajaj, V. S. *Nat. Commun.* **2013**, *4*, 1940.
(9) Pezzagna, S.; Naydenov, B.; Jelezko, F.; Wrachtrup, J.; Meijer, J. *New J. Phys.* **2010**, *12*, 065017.
(10) Laraoui, A.; Meriles, C. A. *ACS Nano* **2013**, *7*, 3403.
(11) Belthangady, C.; Bar-Gill, N.; Pham, L. M.; Arai, K.; Le Sage, D.; Cappellaro, P.; Walsworth, R. L. *Phys. Rev. Lett.* **2013**, *110*, 157601.
(12) Hauf, M.; Grotz, B.; Naydenov, B.; Dankerl, M.; Pezzagna, S.; Meijer, J.; Jelezko, F.; Wrachtrup, J.; Stutzmann, M.; Reinhard, F.; Garrido, J. A. *Phys. Rev. B* **2011**, *83*, 081304(R).
(13) Ofori-Okai, B. K.; Pezzagna, S.; Chang, K.; Loretz, M.; Schirhagl, R.; Tao, Y.; Moores, B. A.; Groot-Berning, K.; Meijer, J.; Degen, C. L. *Phys. Rev. B* **2012**, *86*, 081406.
(14) Laraoui, A.; Hodges, J. S.; Meriles, C. A. *Nano Lett.* **2012**, *12*, 3477.
(15) Jarmola, A.; Acosta, V. M.; Jensen, K.; Chemerisov, S.; Budker, D. *Phys. Rev. Lett.* **2012**, *108*, 197601.
(16) Driehuys, B.; Cates, G. D.; Happer, W. *Phys. Rev. Lett.* **1995**, *74*, 4943.
(17) Thompson, P. A.; Troian, S. M. *Science* **1997**, *389*, 360.
(18) Ortiz-Young, D.; Chiu, H.-C.; Kim, S.; Voïtchovsky, K.; Riedo, E. *Nat. Commun.* **2013**, *4*, 2482.
(19) Zou, Y. S.; Yang, Y.; Zhang, W. J.; Chong, Y. M.; He, B.; Bello, I.; Lee, S. T. *Appl. Phys. Lett.* **2008**, *92*, 053105.
(20) Trusheim, M. E.; Li, L.; Laraoui, A.; Chen, E. H.; Gaathon, O.; Bakhru, H.; Schroeder, T.; Meriles, C. A.; Englund, D. *Nano Lett.* **2014**, *14*, 32.
(21) Natterer, J.; Bargon, J. *Prog. Nucl. Magn. Reson. Spectrosc.* **1997**, *31*, 293.
(22) Theis, T.; Ganssle, P.; Kervern, G.; Knappe, S.; Kitching, J.; Ledbetter, M. P.; Budker, D.; Pines, A. *Nat. Phys.* **2011**, *7*, 571.
(23) Hausser, K. H.; Stehlik, D. *Adv. Magn. Reson.* **1968**, *3*, 79.
(24) Cassidy, M. C.; Chan, H. R.; Ross, B. D.; Bhattacharya, P. K.; Marcus, C. M. *Nat. Nanotechnol.* **2013**, *8*, 363.
(25) London, P.; Scheuer, J.; Cai, J.-M.; Schwarz, I.; Retzker, A.; Plenio, M. B.; Katagiri, M.; Teraji, T.; Koizumi, M.; Isoya, J.; Fischer, R.; McGuinness, L. P.; Naydenov, B.; Jelezko, F. *Phys. Rev. Lett.* **2013**, *111*, 067601.
(26) Koehl, W. F.; Buckley, B. B.; Heremans, F. J.; Calusine, G.; Awschalom, D. D. *Nature* **2011**, *479*, 84.
(27) Riedel, D.; Fuchs, F.; Kraus, H.; Vath, S.; Sperlich, A.; Dyakonov, V.; Soltamova, A. A.; Baranov, P. G.; Ilyin, V. A.; Astakhov, G. V. *Phys. Rev. Lett.* **2012**, *109*, 226402.
(28) Kolesov, R.; Xia, K.; Reuter, R.; Stöhr, R.; Zappe, A.; Meijer, J.; Hemmer, P. R.; Wrachtrup, J. *Nature Commun.* **2012**, *3*, 1029.
(29) Hall, D. A.; Maus, D.; Gerfen, G. J.; Griffin, R. G. *Science* **1997**, *276*, 930.
(30) Ardenkjaer-Larsen, J. H.; Fridlund, B.; Gram, A.; Hansson, G.; Hansson, L.; Lerche, M. H.; Servin, R.; Thaning, M.; Golman, K. *Proc. Natl. Acad. Sci. U.S.A.* **2003**, *100*, 10158.